Applied Energy 358 (2024) 122559

Contents lists available at ScienceDirect

Applied Energy

journal homepage: www.elsevier.com/locate/apenergy

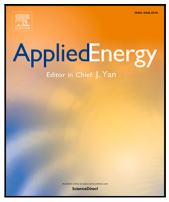

Hydrogen consumption and durability assessment of fuel cell vehicles in realistic driving

M. Piras [a], V. De Bellis [a,*], E. Malfi [a], R. Novella [b], M. Lopez-Juarez [b]

[a] Industrial Engineering Department, Mechanic and Energetic Section, University of Naples "Federico II", via Claudio 21, 80125 Naples, Italy
[b] CMT-Clean Mobility & Thermofluids, Universitat Politècnica de València, Camino de vera s/n, 46022 Valencia, Spain

ARTICLE INFO

Keywords:
Hydrogen
MEA degradation
Predictive energy management strategy
Velocity forecasting
Fuel cell hybrid electric vehicle
Realistic driving conditions

ABSTRACT

This study proposes a predictive equivalent consumption minimization strategy (P-ECMS) that utilizes velocity prediction and considers various dynamic constraints to mitigate fuel cell degradation assessed using a dedicated sub-model. The objective is to reduce fuel consumption in real-world conditions without prior knowledge of the driving mission. The P-ECMS incorporates a velocity prediction layer into the Energy Management System. Comparative evaluations with a conventional adaptive-ECMS (A-ECMS), a standard ECMS with a well-tuned constant equivalence factor, and a rule-based strategy (RBS) are conducted across two driving cycles and three fuel cell dynamic restrictions ($|di/dt|_{max} \leq 0.1$, 0.01, and 0.001 $A/cm^2 s$). The proposed strategy achieves H_2 consumption reductions ranging from 1.4% to 3.0% compared to A-ECMS, and fuel consumption reductions of up to 6.1% when compared to RBS. Increasing dynamic limitations lead to increased H_2 consumption and durability by up to 200% for all tested strategies.

1. Introduction

Fuel cell vehicles (FCVs) powered with H_2 have emerged as a promising solution to the need for reducing greenhouse gas emissions and addressing climate change, as they offer an alternative to traditional gasoline and diesel-powered vehicles [1]. Recognizing the importance of FCVs in the transition to a sustainable and low-carbon energy future, the European Union has developed the European Hydrogen Roadmap, a comprehensive plan that outlines strategies to promote their widespread adoption and drive growth in the hydrogen sector [2]. Heavy-duty vehicles are a significant contributor to greenhouse gas emissions and air pollution [3], and the deployment of hydrogen fuel cell technology has the potential to significantly reduce these emissions. However, extensive research is required to improve the design, performance, and maintenance of FCVs. In fact, the widespread adoption of FCVs is limited by their reduced durability, especially when compared to that of internal combustion engine vehicles. Accurate prediction of fuel cell degradation throughout its lifecycle is a critical aspect for enhancing its durability. By foreseeing degradation, it enables the implementation of alternative control strategies that effectively extend the fuel cell's longevity. Moreover, fuel cell degradation results in a decrease in the FC maximum power output capacity caused by various factors, such as increased activation, ohmic, and concentration losses. Accurately capturing these phenomena is particularly important during dynamic operation when degradation mechanisms are heightened due to load cycling. Based on the aforementioned points, focusing on transport applications, the energy management strategy (EMS), responsible for regulating energy flows and power distribution when both an FC and battery are powering the vehicle, must be aware of the FC degradation rate and state to ensure optimal energy consumption. Different fuel cell states of health (SOH) conscious EMSs have been investigated in the literature [4–6]. However, it is worth noting that a majority of these studies relied on semi-empirical degradation model with constant degradation rates, as proposed by Pei et al. [7]. Despite its simplicity, this model has been widely used to foresee fuel cell stack durability and energy optimization for fuel cell vehicles, either alone [8] or alongside battery degradation models [9]. Its main advantage lies in its quick calculation of performance degradation, enabling advanced techno-economic studies that account for fuel cell degradation effects. However, a limitation of this model is its inability to account for changes in operating conditions and dynamics, quantifying load-change degradation through a linear dependence on the load-change events. This disregards the impact of oscillation frequency on stack temperature and cathode/anode relative humidity, which can significantly influence the degradation mechanisms of the membrane and catalysts.

Considering the typical approach to mitigate fuel cell degradation, which revolves around constraining the dynamics of the FC system to minimize load-change degradation, a previous study conducted by the authors [10] evaluated the potential of a fuel cell range extender

* Corresponding author.
E-mail address: vincenzo.debellis@unina.it (V. De Bellis).

https://doi.org/10.1016/j.apenergy.2023.122559
Received 10 October 2023; Received in revised form 14 December 2023; Accepted 25 December 2023
Available online 5 January 2024

vehicle considering an advanced semi-empirical degradation model developed in [11]. The aim was to enhance FC stack durability and performance through a dynamic control strategy and operational space limitations. However, the study was restricted to the application of a single EMS, which is typically not suitable for real-world driving conditions without proper real-time or iterative adaptation.

Several approaches have been proposed in the literature for optimizing energy management strategies for a realistic implementation, such as fuzzy adaptive EMS [12–14], feedback-based A-EMS [15,16], and forecasting enhanced control strategies [8,17,18]. In particular, this latter approach is being extensively explored in current research. Various methods to predict vehicle speed, including exponentially varying, stochastic Markov chain, and neural network-based velocity prediction are available for integration into the EMS [19]. In a study conducted by Zhou et al. [20], a multi-criteria power allocation strategy was proposed for an FCHEV, aiming to improve its operational efficiency. The strategy comprised an adaptive online-learning enhanced Markov velocity-forecast approach. The findings indicated a reduction in hydrogen consumption by approximately 12%, though certain limitations exist within this methodology. Specifically, the velocity predictor's training dataset was composed of a sequence of driving cycles having different driving patterns (highway/suburban/urban). The use of standard driving cycles might not be fully representative of real-world driving, since those cycles might lack of highly impulsive accelerations/decelerations and transient maneuvers. Moreover, the variations observed in real-world driving patterns due to factors like traffic, weather, and driver behavior are not completely considered in standardized driving cycles. Therefore, developing and testing vehicle predictive control strategies based on standard driving cycles might not fully reflect the diverse range of driving conditions that vehicles encounter in real-world usage. Sun et al. [21] introduced a real-time optimal EMS for a bus application that utilizes driving characteristics recognition and density-based spatial clustering of applications with a noise algorithm to forecast the co-state variable. The results showed a reduction in hydrogen consumption by 6.6% and a SOC fluctuation range of less than 2% compared to a rule-based strategy. However, this EMS was only tested on selected and fixed bus routes.

In the literature, some studies have addressed these limitations by incorporating a velocity predictor trained and validated under real-world driving conditions, as exemplified in [22]. However, in this particular case, the EMS is only verified on two standard driving cycles, the WLTC and the NEDC. Especially the latter does not serve as a suitable test case for evaluating the effects of dynamic limitations on the fuel cell in an FCHEV since it is a highly simplified driving cycle. Some studies have thus attempted to integrate these prediction techniques for investigations on fuel cell vehicles, also analyzing their impact on degradation. The approach presented in [17] introduces a reinforcement learning-based EMS for a fuel cell/lithium battery hybrid system. The proposed method demonstrates significant advantages, achieving a reduction in fuel cell life decay rate and an improvement in fuel economy of up to 6% compared to conventional methods. The paper [8] introduces an EMS based on MPC integrated with a vehicle speed predictor for fuel cell electric vehicles, where the future vehicle total power demand is forecasted using a Markov speed predictor and incorporated into the energy management system response prediction model. The proposed approach achieves a 3.74% reduction in total operation cost compared to a normal MPC strategy and a 1.39% reduction compared to the speed prediction dynamic programming strategy. In both the aforementioned cases, however, the velocity predictor is constructed based on standard driving cycles, and the fuel cell degradation is evaluated using a low-fidelity model that does not allow for a detailed investigation of the contribution of different degradation sources.

This reveals a knowledge gap in terms of both the analysis and comparison of different EMSs enhanced by velocity prediction and the evaluation of the trade-off between hydrogen consumption and fuel cell durability, using a reliable degradation model, all under realistic driving conditions. In this perspective, this work investigates the impact of different dynamic restrictions for a predictive ECMS (P-ECMS) on fuel consumption and FC stack durability, in comparison to a conventional proportional controller-based adaptive-ECMS (A-ECMS), the standard ECMS (S-ECMS) with a properly tuned constant equivalence factor, and a rule-based strategy (RBS) over two different driving cycles and three restrictions on the fuel cell (FC) dynamics ($|\mathrm{di/dt}|_{max} \leq 0.1$, 0.01, and 0.001 $\mathrm{A/cm^2\ s}$). The primary challenge encountered in this study was to effectively integrate the vehicle model, the semi-empirical degradation model, and the velocity predictor-enhanced EMS in a parallel manner to simulate real-world driving conditions.

1.1. Knowledge gaps

Grounding on the above literature review, some considerations can be drawn, collecting the knowledge gaps to be faced in the field of neural network-based predictive energy management strategy for FC-powered vehicles that estimates and favors FC durability:

1. Studies assessing fuel cell degradation during real-world driving cycles often employ empirical models that may not capture the full thermodynamic effects and/or the individual contributions of degradation sources [8,17,23,24].
2. In the existing literature, the investigation of adaptive/predictive EMSs' impact on FC degradation for realistic heavy-duty applications does not extensively focus on a detailed examination of fuel cell durability while comparing the effects of different dynamic restrictions across various control strategies [20,25].
3. In general, for studies on FCVs, predictive control strategies with a predictor module often depend on driving cycle predictors that are trained and/or evaluated using standardized driving cycles [26–28]. Nevertheless, these standardized cycles frequently fail to mirror the driving patterns observed in transient, real-world scenarios. Consequently, the EMS lacks verification in simulations under realistic situations.
4. Studies focusing on realistic driving conditions frequently concentrate on bus transportation or fixed route scenarios, failing to validate the findings in realistic driving situations involving diverse road types [21,29–32].

1.2. Contribution and objectives

Based on the considerations in the previous section, it is evident that the effect of a predictive EMS on the durability and performance of FC systems (FCS) when imposing restrictions over the dynamics has not been fully explored yet for heavy-duty FCVs. For this reason, the novelty of this paper lies in evaluating the influence of various dynamic restrictions on fuel consumption and FC stack durability using an advanced degradation model under real-world driving conditions for a P-ECMS while comparing this with three different EMSs. This study aims to accomplish its objectives by employing a validated FCS model that includes a fully optimized balance of plant and that is validated across different operating conditions. Additionally, a velocity predictor module has been integrated into the P-ECMS, which was trained using realistic driving data. To achieve this, the study aims to fulfill the following partial objectives:

- Integrate the P-ECMS in a full heavy-duty FCV.
- Identify the sensitivity of the P-ECMS to the initial equivalence factor and its update gain value depending on the dynamic restriction.
- Compare the proposed P-ECMS to a traditional A-ECMS, a real-time implementable rule-based strategy, and the standard off-line

Table 1
Main characteristics of the tested FCHEV, based on the Hyundai XCIENT FCV [33].

Fuel cell hybrid electric vehicle features	
Vehicle	
Mass (vehicle+cargo), kg	18 000
Car aero drag, m^2	9.38
Wheel diameter, m	0.513
Axle ratio, –	4.875
Fuel cell stacks	
Cells number, –	480
Max power, kW	120
Max efficiency, –	0.62
DC–DC efficiency, –	0.95
Electric machine	
Max power, kW	350
Max torque, N m	3400
DC-AC efficiency, –	0.95
Battery	
Rated capacity, Ah	110.55
DC–DC efficiency, –	0.95
Rated maximum power, kW	400
Gearbox	
Gear 1 ratio, –	4.484
Gear 2 ratio, –	2.872
Gear 3 ratio, –	1.842
Gear 4 ratio, –	1.414
Gear 5 ratio, –	1.000
Gear 6 ratio, –	0.742

tuned ECMS (S-ECMS), in terms of battery charge sustenance, H_2 consumption, and membrane electrode assembly (MEA) degradation.
- Identify the contribution of each degradation source in realistic driving conditions due to the different EMSs and analyze the change of the weight of each source when changing the dynamic restriction.

2. Modeling framework

In this section, the models used for the simulation of the HDDT and the realistic driving cycles are explained. The modeling framework consists of a heavy-duty vehicle model (Section 2.1), in which the powertrain is a validated FCS integrating both the FC stack and the balance of plant or BoP (Section 2.2) complemented by a semi-empirical FC degradation model designed to estimate the FC degradation rate by source in driving conditions (Section 2.3).

2.1. Vehicle model

The architecture under study is multi-FC system heavy-duty vehicle, whose main features are collected in Table 1. This vehicle is simulated GT-Suite 2020 software by a dynamic model. The powertrain is composed of two fuel cell systems, a battery pack, DC–DC converters, an electric motor, a gearbox, and a differential, as depicted in Fig. 1. To prevent electrical oscillations from the DC bus hence causing damage to the FC system, an indirect electronic configuration was selected, which facilitates the downsizing of the FC system, consistently with contemporary FCVs. The battery pack was modeled using the equivalent circuit method, which accounts for SOC-dependent internal resistance and open-circuit voltage. The efficiency of the electric machine was determined based on a torque–speed map. Further information about the fuel cell stack model is discussed in the subsequent section. The gear shifting is regulated by a speed-accelerator pedal position lookup table.

2.2. Fuel cell system model

The FCS was modeled according to [34,35]. The FC is characterized by its polarization curve, where the relationship between current density and voltage is modeled the following set of equations:

$$V_{FC} = V_{OC} - V_{act} - V_{ohm} - V_{mt} \tag{1}$$

$$V_{OC} = \frac{-\Delta \overline{g}_f}{2F} \tag{2}$$

$$V_{act} = \begin{cases} \frac{R_{gas}T}{2F}\left(\frac{i}{i_0}\right) \\ \frac{R_{gas}T}{2\alpha F} ln\left(\frac{i}{i_0}\right) \end{cases} \tag{3}$$

$$V_{ohm} = RI \tag{4}$$

$$V_{mt} = -C\, ln\left(1 - \frac{i}{i_l}\right) \tag{5}$$

where V_{OC} is the open voltage circuit and V_{act}, V_{ohm} and V_{mt} are the activation, ohmic, and mass transport losses. Incorporating the change in the ionic conductivity of the membrane in relation to its water content, temperature, and properties, the ohmic resistance (R_{ohm}) was modeled using the approach outlined in [36]. The exchange current density is determined by the FC temperature, oxygen partial pressure, electrochemical activation energy, electrode roughness, and reference exchange current density $i_{0,ref}$, as discussed in [37]. To validate the model under different conditions of pressure and temperature, the reference exchange current density, reference ohmic resistance, charge transfer coefficient (α), mass transport loss coefficient (C), limiting current density (i_l), and voltage open circuit losses values were calibrated using the GT-Suite genetic algorithms toolbox, based on experimental data from [38,39]. Unlike other studies, this FC model was validated by simultaneously matching various numerical polarization curves to experimental data under different levels of pressure and temperature. This validation process is essential for driving cycle conditions, where the FC stack is subject to various operating conditions depending on external environmental factors and the operation of the auxiliary components. The synthetic validation results showed an overall RMS deviation below 2%.

The FC model was then integrated with individual models for each one of the auxiliary components that are required to supply and condition the flows required by the stack in a powertrain, i.e., the BoP, thus constituting the FCS (Fig. 2). This set of models includes the entire anode and cathode circuits, their conditioning, and a cooling system. The anode circuit is composed of the H_2 tank with a pressure-regulating valve connecting it to the stack and an active recirculation circuit in which the anode stoichiometry is controlled by means of a H_2 pump. The cathode namely consists of an electric compressor, a heat exchanger placed downstream of the compressor, a humidifier at the stack inlet and an exhaust valve to control the cathode pressure. The operation of these components was optimized in previous studies to ensure that the FCS net efficiency (FC stack minus BoP consumption) is maximized at each current density [34]. To speed up the computational time, some simplifications of the FC model were introduced, leading to the mean value model actually adopted in this research work. Notwithstanding some minor misalignments, the reduced model accurately replicates the actual FC system operation with simplified dynamics, offering higher fidelity results than other approaches that oversimplify the entire FC system to a single polarization curve, which neglect BoP power demand and inefficiencies associated with driving cycle conditions. The mean values model yields slightly lower hydrogen consumption by operating in pseudo-steady conditions because it does not consider inefficiencies linked to transient operation, such as slow thermal dynamics. Additionally, the energy usage distribution in both models showed a notable deviation only in FC system losses due to model simplification. For other purposes such as generating brake power or charging the battery with the FC stack, the energy usage is almost identical. Despite the relatively low deviation, it is deemed

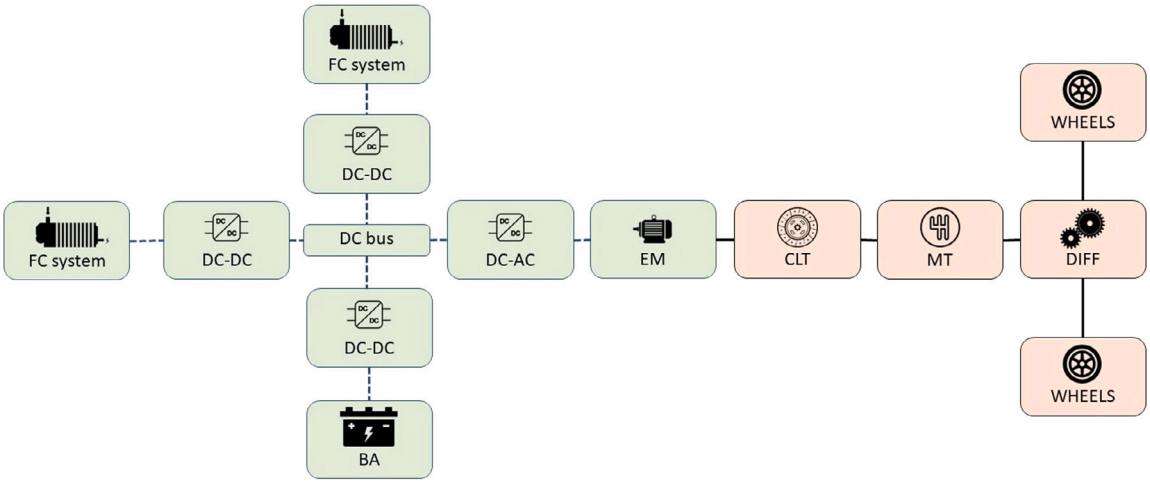

Fig. 1. Heavy-duty fuel cell hybrid electric vehicle powertrain scheme.

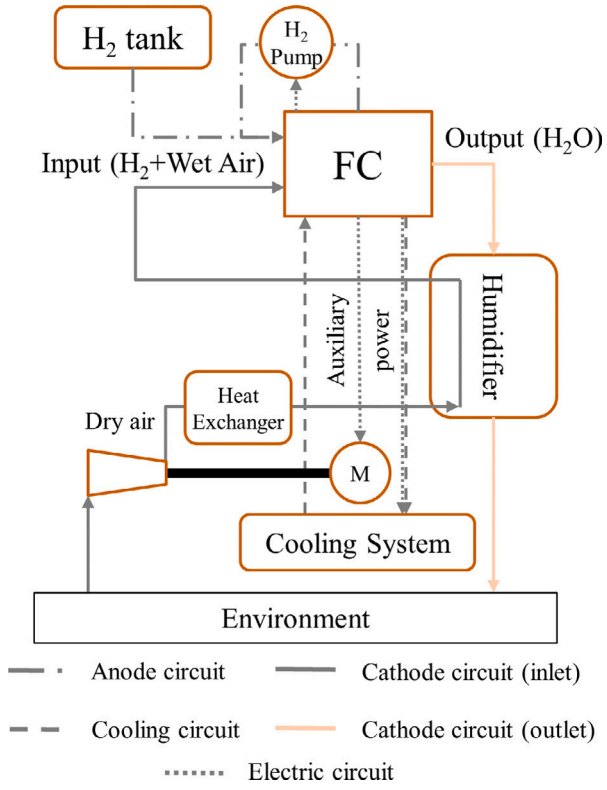

Fig. 2. Fuel cell system outline.

acceptable to reduce computational costs from 4 h to 50 s per case. For a more in-depth examination of the BoP, the reader can refer to [34].

2.3. FC degradation model

Fuel cell degradation is influenced by how it is operated (EMS) and the conditions of temperature, pressure and relative humidity under which it operates. The degradation sources could arise from different electrochemical mechanisms that are active at low-load, medium-load (natural), high-load or load-change conditions. These mechanisms depend on the voltage at which each cell operates and the flow of protons through the membrane, which determines the rate of the primary electrochemical processes within the FC stack and which is proportional to the current density. The degradation rate exerted from these phenomena is affected by water presence (RH) and the operating temperature (T) in both the cathode and the anode.

Table 2
Reference degradation rates (1st layer) to be scaled.

Condition	δ [fraction V loss]
Low power [/h] $\left(\frac{d\delta}{dt}\vert_{lp,ref}\right)$	$1.26 \cdot 10^{-5}$
Load change [/cycle] $\left(\frac{d\delta}{dn_{lc}}\vert_{ref}\right)$	$4.94 \cdot 10^{-7}$
High power [/h] $\left(\frac{d\delta}{dt}\vert_{hp,ref}\right)$	$1.03 \cdot 10^{-5}$
Start-stop [/cycle] $\left(\frac{d\delta}{dn_{ss}}\vert_{ref}\right)$	$1.96 \cdot 10^{-5}$

This degradation model is formulated as scaling functions to predict the underlying changes in the degradation mechanisms when the FC stack is subjected to different operating conditions. These functions are applied over degradation rate coefficients estimated under reference levels of i, T, and RH, according to the experiments in [7]. The coefficients are here adjusted to calibrate the degradation model (see Table 2). For more details about the adopted degradation model, the reader can refer to [11].

The model expresses degradation as a voltage degraded ratio $\delta = 1 - V_{deg}/V_{FC}$, where V_{FC} and V_{deg} are the non-degraded and degraded FC stack voltage, respectively. It modifies the reference degradation rates in Table 2 to predict the evolution of δ with time, depending on the operating conditions and the electrochemical phenomena:

$$\delta = \int_0^t \left[\left.\frac{d\delta}{dt}\right|_{lp} + \left.\frac{d\delta}{dt}\right|_{lc} + \left.\frac{d\delta}{dt}\right|_{hp} + \left.\frac{d\delta}{dt}\right|_{nt} \right] dt + \frac{d\delta_{ss}}{dn_{ss}} n_{ss} \tag{6}$$

$$\left.\frac{d\delta}{dt}\right|_{lp} = \left.\frac{d\delta}{dt}\right|_{lp,ref} \cdot \xi_{lp}(i) \cdot \tau(T) \cdot \eta(\overline{RH}) \tag{7}$$

$$\left.\frac{d\delta}{dt}\right|_{lc} = \left.\frac{d\delta}{dn_{lc}}\right|_{ref} \cdot \xi_{lc}\left(\frac{di}{dt}\right) \cdot \tau(T) \cdot \eta(\overline{RH}) \tag{8}$$

$$\left.\frac{d\delta}{dt}\right|_{hp} = \left.\frac{d\delta}{dt}\right|_{hp,ref} \cdot \xi_{hp}(i) \cdot \tau(T) \cdot \eta(\overline{RH}) \tag{9}$$

$$\left.\frac{d\delta}{dt}\right|_{nt} = \frac{\left.\frac{d\delta}{dt}\right|_{hp,ref} \xi_{hp}(i_{hp}) - \left.\frac{d\delta}{dt}\right|_{lp,ref} \xi_{lp}(i_{lp})}{i_{hp} - i_{lp}} (i - i_{lp}) + \left.\frac{d\delta}{dt}\right|_{lp,ref} \xi_{lp}(i_{lp}) \tag{10}$$

$$\frac{d\delta_{ss}}{dn_{ss}} = \left.\frac{d\delta}{dn_{ss}}\right|_{ref} \tag{11}$$

where ξ, τ and η are scaling functions modulating the degradation rates according to the current density (electrochemical mechanism), temperature, and relative humidity, respectively. i denotes the current

density, i_{hp} and i_{lp} are the high-power and low-power current densities, respectively, and n_{ss} is the number of start-stop cycles. These parameters and functions are used in the degradation model to compute the change in the voltage degraded ratio (δ) when the FC is subjected to low-power conditions ($\frac{d\delta}{dt}|_{lp}$), where the high cell potential implies the activation of degradation mechanisms affecting the catalyst layer, to load-change operation ($\frac{d\delta}{dt}|_{lc}$), in which the water and flow management may cause certain deterioration to the MEA, to high-power condition ($\frac{d\delta}{dt}|_{hp}$), in which the FC operates at high temperature and the intensity of the degradation mechanisms increase, to natural decay ($\frac{d\delta}{dt}|_{nt}$) and to start-stop conditions ($\frac{d\delta}{n_{ss}}$).

The scaling functions are expressed as:

$$\xi_{lp}(i) = \begin{cases} \xi_{lp}(i) = -0.176 \cdot \ln i + 0.169 & i \le i_{lp} \\ 1 & i > i_{lp} \end{cases} \tag{12}$$

$$\xi_{lc}\left(\frac{di}{dt}\right) = \frac{|\Delta i|_{dt}}{2\,|\Delta i|_{ref}} \tag{13}$$

$$\xi_{hp}(i) = \begin{cases} \frac{i}{i_{hp}} & i > i_{hp} \\ 1 & i \le i_{hp} \end{cases} \tag{14}$$

$$\tau(T) = \tau(T) = -5.390 \cdot 10^{-4} T^2 + 0.399 \cdot T - 71.576 \tag{15}$$

$$\eta(\overline{RH}) = 0.10646 e^{0.028 \cdot RH\ [\%]} \tag{16}$$

where τ is valid in the range $T \in [310, 373.15]$ K following the change in the fluoride release rate and the electrical surface area according to [40,41] respectively. η was obtained from the experimental results of [42] that served to identify the FC degradation during voltage cycling under different levels of RH.

This model was validated with data from a bus operating on a real daily route retrieved from [7] in previous studies [11] and has been applied successfully to predict the change in the degradation rate and the relevance of each FC degradation source in other studies [10].

3. Energy management strategy

3.1. Equivalent consumption minimization strategy

The EMS has integrated the ECMS algorithm as its core framework. It is an optimization algorithm commonly used in EMS for hybrid electric powertrains. Its main goal is to minimize the equivalent fuel consumption of a vehicle by dynamically controlling the power split between the battery and the FCS in real time while ensuring that the battery SOC remains within a desired range. This is accomplished by converting electricity consumption into a corresponding amount of fuel and then distributing power to minimize the equivalent fuel consumption according to:

$$J = \dot{m}_f + s\frac{P_{batt}}{LHV} + \lambda \tag{17}$$

where P_{batt} and $\dot{m}_f$ respectively are the net electrical power as measured at the battery terminals and the current fuel rate. LHV and s denote respectively the lower heating value of the fuel and the equivalence factor, representing the cost of the electrical power exchanged with the battery. Lastly, λ represents a cost term that imposes restrictions on the FC dynamic behavior discarding solutions that imply a dynamic higher than desired. It can be expressed as:

$$\lambda = \begin{cases} 0 & |di/dt|(t+dt) \le |di/dt|_{max} \\ inf & |di/dt|(t+dt) > |di/dt|_{max} \end{cases} \tag{18}$$

The objective of this study is to minimize H_2 consumption while maintaining the battery SOC in a charge-sustaining mode. This implies that the amount of energy used from the battery during the cycle must be equal to the amount of energy replenished into it, resulting in a net zero change in SOC. The implications of applying different stack dynamics are discussed in detail in Section 5.

3.1.1. Role of the equivalent factor and A-ECMS

The ECMS is strongly influenced by the equivalence factor to ensure adequate battery charge-sustaining capability. Determining its appropriate value is greatly influenced by the driving conditions, and knowledge of the driving mission beforehand is necessary to establish a constant equivalence factor for achieving optimal control. However, when the driving cycle is unknown beforehand, a fixed equivalence factor may not be sufficient to guarantee battery charge sustainability in practical applications. To address this issue, an adaptive equivalence factor that can vary according to the driving conditions may be more effective in maintaining the battery SOC. The A-ECMS approach is based on the iterative updating of the equivalence factor using a feedback-oriented law that adjusts the equivalence factor based on the error between the reference SOC value and the real-time feedback SOC value. The adaptation law proposed in [43] is used as a benchmark in this study.

$$s_{n+1} = s_n + k_p(SOC_{ref} - SOC_n) \tag{19}$$

where SOC_{ref} is the reference SOC value, SOC_n and s_n are the SOC and the EF at time $t = n$, k_p is a fixed control gain and s_{n+1} is the EF at the following time step $n + 1$. It should be noted that during charge-sustaining operations, the reference SOC remains constant. For this study, the equivalence factor is updated at a rate of 1 s per sample. As demonstrated in the results section, the effectiveness of the adaptive ECMS approach is heavily reliant on both the initial value of the EF and the update rate parameter (k_p).

3.2. Velocity forecasting layer

To implement the P-ECMS, the integration of a velocity predictor is essential. To this aim, an LSTM neural network velocity predictor, developed in a previous work [44], is employed. It presents three LSTM layers with 128 neurons and one dense layer. LSTM neural networks are a type of recurrent neural network that utilizes a memory component to address the vanishing gradient problem. These networks have proven to be effective in dealing with sequential data, such as audio, text, and video [45], and have been widely used in research related to multivariate and multi-input predictions [46]. The velocity predictor is implemented in Matlab, utilizing the adaptive moment estimation (ADAM) optimizer with a learning rate of 0.00611 for neural network training. Extensive sensitivity analysis on the neural network parameters, conducted with real-world driving data, validates that the proposed neural network achieves prediction accuracy comparable to previous literature [30,47–49]. According to previous results and studies in the literature [50] the historical sequence length (H_s) is fixed as 10 s and the forecasting horizon (H_f) is fixed as 20 s. Further elaboration on these aspects is provided in the previous work [44]. The predictor takes a series of three historical features as input: the vehicle's velocity, acceleration, and distance to the next intersection or traffic light. The distance is calculated by utilizing data from the map service provider:

$$d_{jt} = \frac{D_j - \int_{t_j}^{t-t_j} v dt}{D_j}, t \in [t_j, t_{j+1}] \tag{20}$$

where d_{jt} is the distance feature from the intersection j to the intersection j+1, D_j is the distance from the intersection j to the intersection j+1, and t_j is the FCV arrival time at the intersection j. Real driving data simulated by GT-Real Drive, which generated routes based on TEN-T routes where heavy-duty FCVs are expected to move, was utilized to train and test the neural network. GT-Real Drive is a powerful tool that incorporates various factors such as live or historical traffic conditions, time of day and week, traffic signals, driver preferences, and via points to create realistic driving scenarios. Starting and destination points are the only inputs required. The dataset was generated by selecting six different routes (Table 3) that link nodes of the TEN-T, considering

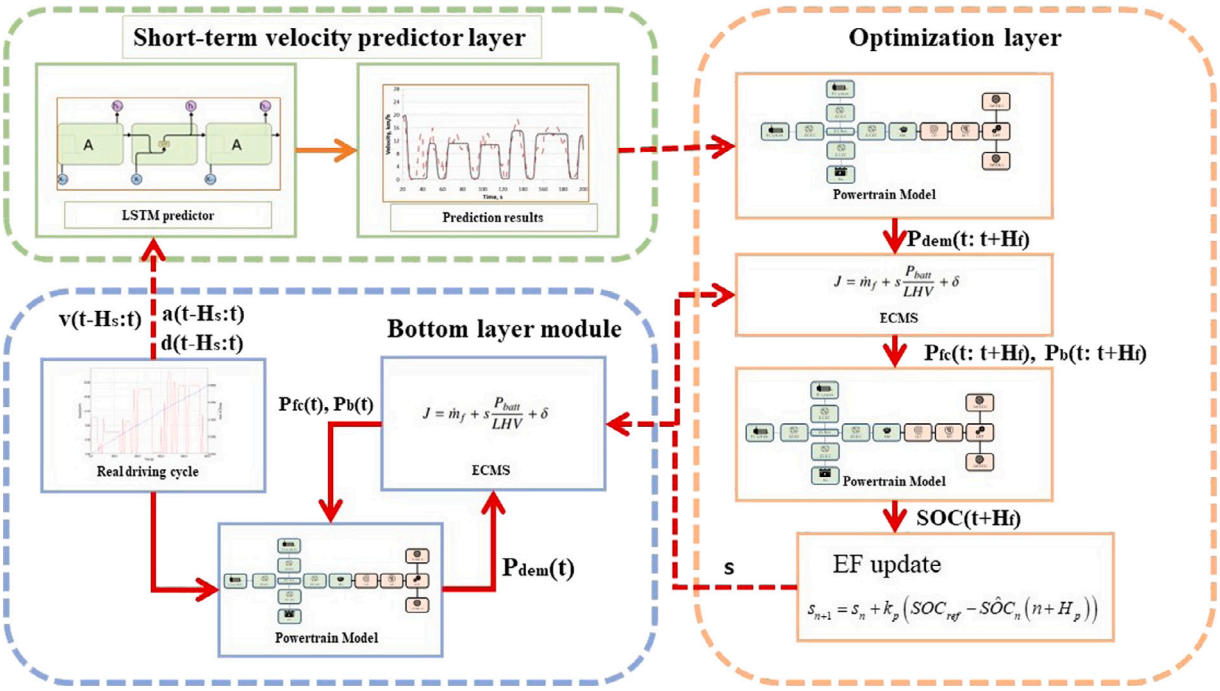

Fig. 3. Framework of the Predictive-EMS.

Table 3
TENT-T routes for the dataset generation.

Route	Country	Distance, km	Mean speed, km/h	Mean acceleration, m/s^2	Max acceleration, m/s^2	Max deceleration, m/s^2	Mean deceleration, m/s^2
Budapest Tatabánya	Hungary	60	62.3	0.18	2.24	−3.81	−0.19
Fiumicino Civitavecchia	Italy	71	67.4	0.49	2.32	−3.19	−0.56
Hamburg Ahrensburg	Germany	34	27.9	0.76	2.33	−3.23	−0.95
Paris Rouen	France	143	61.5	0.32	2.32	−3.27	−0.34
Sevillia Algeciras	Spain	184	59.1	0.86	2.32	−3.23	−1.14
Ventspils Riga	Latvia	184	36.7	0.94	2.32	−3.25	−1.25

Table 4
Test cases definition.

Route	Country	Distance, km	Mean speed, km/h
HDDT	–	37.2	64.2
Bucarest Giurgiu	Romania	62	39

different speed profiles to verify the algorithm's suitability for a broad range of driving conditions. Combining GT-Real Drive with the TEN-T provides accurate driving information for key roadways throughout Europe, leading to a reliable EMS for actual heavy-duty vehicle usage. Before training, the dataset is standardized, and 90% of the data is used for training while the remaining 10% is utilized for testing.

3.3. Predictive ECMS

Chen et al. [51] suggested the subsequent EF adaptation law to enhance the performance of the A-ECMS [43]:

$$s_{n+1} = s_n + k_p(SOC_{ref} - \hat{SOC}_n(n + H_p)) \tag{21}$$

In contrast to Eqs. (19), (21) updates the EF with feedback on the short-horizon predicted future SOC ($\hat{SOC}_n(n+H_p)$). In [51], the impact of a realistic velocity prediction is not studied, and the future velocity is considered as an external input. Furthermore, the authors applied their EMS to a hybrid electric vehicle equipped with an internal combustion engine, which does not have the same dynamic limitations as an FCS due to membrane degradation. This study addresses this knowledge gap by integrating the adaptation law of Eq. (21) into the multi-level control strategy depicted in Fig. 3. The EMS works as follows:

1. The velocity forecasting layer predicts the vehicle velocity H_f seconds ahead.
2. The predicted velocity is transmitted to the powertrain model, which uses instantaneous Hamiltonian minimization to forecast a SOC trajectory for H_f seconds in the future considering the EF value of the previous iteration.
3. The EF is then updated according to Eq. (21), based on the discrepancy between the reference SOC and the predicted SOC
4. The updated EF is sent to the bottom layer, which solves the ECMS in the time window $[t, t + H_f]$, and the process repeats from step 1 using the updated EF as the value for the subsequent iteration.

The procedure to select the initial EF for the first iteration is described in the Results section. The EF update time step is equivalent to H_f. The advantages of this approach are discussed in the results section.

4. Simulations

Table 4 lists the two driving cycles that were chosen to investigate the capabilities of the proposed P-ECMS. In this perspective, the P-ECMS is compared to the standard ECMS (S-ECMS) with a constant and optimal equivalence factor, the A-ECMS (which follows the adaptation law provided by Eq. (19)), and a rule-based EMS (abbreviated

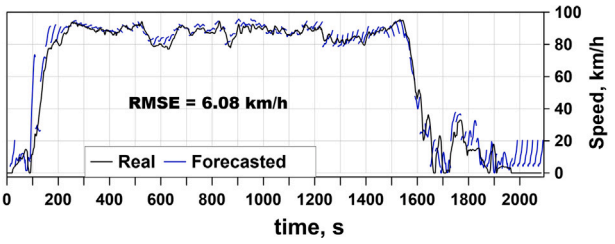

Fig. 4. Speed forecasting in the driving cycle HDDT.

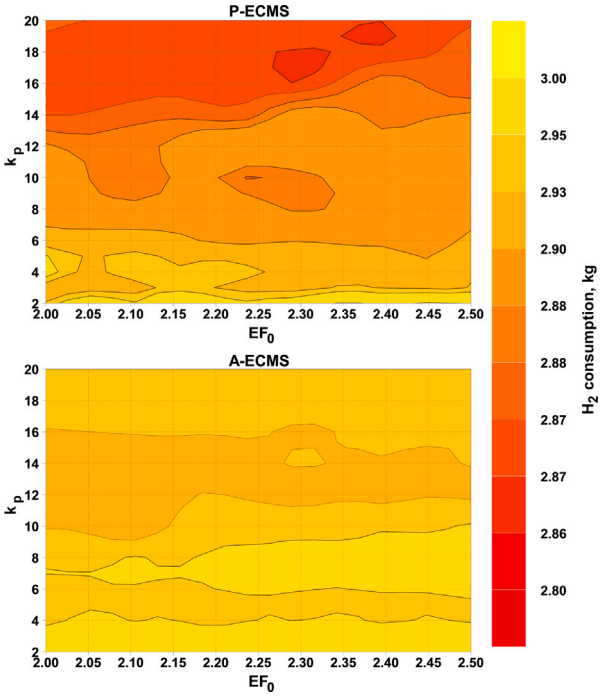

Fig. 5. Corrected hydrogen consumption distribution for P-ECMS and A-ECMS.

as RBS) [52], where the control is determined according to the FCS efficiency map. It is worth noting that these test cases were not included in the neural network's training dataset, so the P-ECMS was tested on unfamiliar driving conditions. To adhere to range-extender designs, the simulations' starting SOC was set to 30%. To calibrate both the A-ECMS and P-ECMS optimally, the initial value of EF (EF_0) and k_p (see Eqs. (19) and (21)) needed to be identified. In the following section, a sensitivity analysis is performed for the HDDT cycle to determine the optimal calibration by analyzing the impact of varying k_p (in the range [2,20]) and EF_0 (in the interval [2,2.5]) on the terminal SOC and hydrogen fuel consumption. The EF was updated using Eqs. (19) and (21) in the range [1.5,3]. The RBS, on the other hand, did not require any initialization parameter. The performance of each EMS has been evaluated using three different stack current dynamic restrictions: 0.1, 0.01, and 0.001 A/cm^2 s (λ in Eq. (17)). The first restriction of 0.1 A/cm^2 s represents a highly dynamic case, while the second restriction of 0.01 A/cm^2 s was implemented to prevent cathode/anode starvation. This restriction was found to preserve highly dynamic operation while promoting stability and maintaining stoichiometry close to target values. The last restriction of 0.001 A/cm^2 s represents a high level of dynamic restriction where minimum degradation of the fuel cell is expected.

5. Results and discussion

Initially, a comprehensive examination of the results obtained from the HDDT driving cycle is conducted in this section, followed by an assessment of the case concerning the realistic driving cycle. The H_2 consumption represents a corrected fuel mass taking into account the energy variations in the battery. This choice is necessary to have consistent comparisons between cases with different final battery SOC. The battery energy is converted into an equivalent H_2 mass according to:

$$H_{2,eq} = \mathrm{H}_2 - \frac{\Delta E_b}{\overline{\eta_b}\,\overline{\eta_{FCS}}\,LHV_{\mathrm{H}_2}} \tag{22}$$

where (ΔE_b) is the battery energy imbalance, $\overline{\eta_b}$, $\overline{\eta_{FCS}}$ respectively represent the battery and FCS efficiencies, and (LHV_{H_2}) is the H_2 lower heating value.

It is critical to highlight that preliminary analyses in the lowest dynamic case ($|\mathrm{di/dt}|_{max}$ = 0.001 A/cm^2 s) have revealed that the battery SOC may fall below or exceed the acceptable thresholds due to the strong dynamic restrictions. Consequently, in this case, to enable the fuel cell system to respond with high dynamics in adverse conditions that may damage the battery or hinder the completion of the driving mission, the maximum current derivative is corrected as:

$$|di/dt|_{max} = \begin{cases} 0.001 & 0.25 < SOC < 0.35 \\ 0.1 & otherwise \end{cases} \tag{23}$$

5.1. HDDT driving cycle

Fig. 4 portrays the outcomes of the velocity predictor. The neural network's performance is superior in circumstances where there are variations in speed, but it displays more significant inaccuracies during the acceleration and deceleration phases. The velocity RMSE of 6.08 km/h confirms the accuracy of the speed forecasting algorithm.

As previously explained, the A-ECMS and P-ECMS require the definition of k_p and EF_0. For this reason, the HDDT cycle was considered as a reference case for defining these parameters for the three different $|\mathrm{di/dt}|_{max}$. The same k_p and EF_0 were then used for the Bucharest-Giurgiu cycle. This selection is intended to assess the EMS's robustness under various driving conditions. The HDDT cycle was adopted as the benchmark for optimization. As demonstrated in this section, this choice obviates the need to define different EF_0 for different driving missions. For the sake of simplicity, only the sensitivity analysis results for the $|\mathrm{di/dt}|_{max}$ = 0.1 A/cm^2 s case are described below. The same considerations apply to the other two cases with slower FC dynamics. The P-ECMS leads to lower corrected hydrogen consumption compared to the A-ECMS for every pair of EF_0 and k_p parameters, owing to its ability to access future information in the short forecasting horizon (as depicted in Fig. 5). Additionally, H_2 consumption is primarily influenced by the value of k_p for both adaptive strategies, while the effect of EF_0 is comparatively minor. The final SOC tracking error, as shown in Fig. 6, is also subject to the same considerations. Notably, for low values of k_p, the P-ECMS incurs a significantly higher error than the A-ECMS. This disparity arises from the distinct update times of the EF: while the A-ECMS adapts the EF every second, the P-ECMS updates it every H_f seconds. The latter update frequency was chosen to simplify the strategy and reduce computation times, without increasing the error on the final SOC tracking for higher k_p values, where H_2 consumption is generally lower in the relevant region of the maps. The distribution of the percentage increase in corrected H_2 consumption of the A-ECMS relative to the P-ECMS is presented in Fig. 7. It is evident that, for equivalent values of k_p and EF_0, the P-ECMS delivers a lower fuel consumption for each parameter pair, with the greatest reduction being approximately 3%, namely due to the additional information provided by the speed forecast. Then, the values of k_p and EF_0 that minimize H_2 consumption, while keeping the terminal SOC tracking error below 1% (when possible), for both the P-ECMS and the A-ECMS

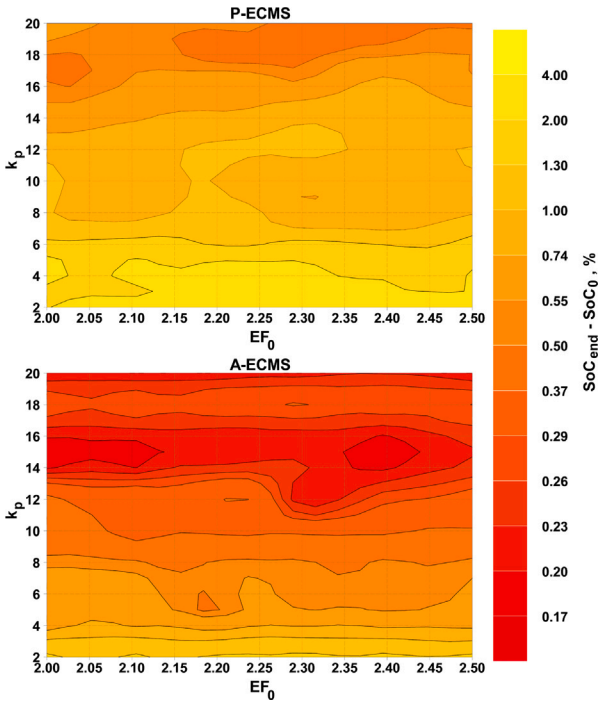

Fig. 6. Terminal SOC tracking error distribution for P-ECMS and A-ECMS.

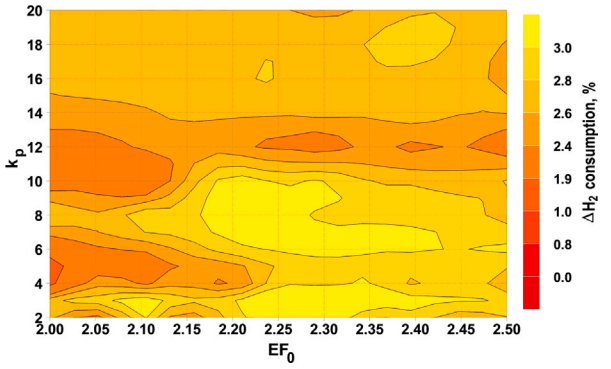

Fig. 7. Hydrogen consumption percent difference between P-ECMS and A-ECMS. A positive percentage number indicates that A-ECMS leads to greater hydrogen consumption than P-ECMS.

have been selected. Hence, a comprehensive analysis and comparison of the simulation results obtained for the four tested strategies with the corresponding optimum values of k_p and EF_0, when applicable, are provided.

Figs. 8 and 9 depict the comparison of time evolution SOC, FC current density, and EF for different FC dynamic limitations. For the sake of clarity, the RBS results are not included in the figure, while its general results are depicted in Figs. 11, 12, 13 and discussed in the following. Fig. 8d and f clearly demonstrate that severe limitations in the FC dynamics to values of 0.01 A/cm^2 s and 0.001 A/cm^2 s result in significant changes to the evolution of current density along the cycle. As a consequence, significant impacts both on H_2 consumption and FC stack durability are expected. The FC stack reaches its maximum current density less frequently. This may result in an increase in medium-power or natural degradation to compensate for the decrease in the SOC when high power is demanded by the electric motor. Additionally, the intensity of load-change is evidently affected (rate of change and amplitude of the load-change oscillations), implying an overall reduction in the total degradation rate since the primary source of degradation, which is load-change, is directly targeted. The effect over durability should be determined by taking into account the FC stack physical conditions, not only the current density evolution, but the decrease in the load-change degradation of such significance has positive effects over FC durability. Fig. 8e and f highlight a drop in the current density around the 1700 s because of the excessively high SOC and a sudden increase in the current density around 300 s in the A-ECMS since the SOC reaches the lower limit 0.25. This justifies the adaptive change in the dynamic limits to improve SOC sustenance (Eq. (23)). The different time evolution of current density between P-ECMS and A-ECMS is justified by the different evolution of the equivalence factor because of the forecasting ability of the P-ECMS and the different updating frequencies (Fig. 9). This also has an impact on the power distribution between the fuel cell and the battery (Fig. 10). Fig. 10 also highlights that as the limit on the current derivative decreases, the fuel cell tends to operate at nearly constant power, while the battery handles the dynamic power demand.

Except the S-ECMS, the P-ACMS, A-ECMS, and RBS sustain the battery SOC around the target value of 30%. The charge sustenance deteriorated in the case of low dynamics (Fig. 11). Thanks to the velocity prediction and the enhanced EF adaptation, the P-ECMS reduces H_2 consumption compared to the A-ECMS and the RBS (Fig. 12) with only an increase of 1.7% with respect to the S-ECMS. Note that in Fig. 12 the value above the bars represents the increase in the H_2 consumption compared to the S-ECMS working with high current dynamics. For any EMS, increasing the dynamic limitation to 0.01 and 0.001 A/cm^2 s rises H_2 consumption by 1%–3% compared to applying the same EMS with high FC dynamics. On the other hand, the FC stack durability is increased by up to 2.24 times with respect to the S-ECMS case with high dynamics, which proves that the P-ECMS can be used effectively with low dynamics to improve the FC durability. In general, all the EMS offer high durability when the dynamic restriction is high (see Fig. 13), and the differences are mainly motivated by the current density evolution and its impact on the physical conditions. For instance, using the S-ECMS implies lower levels of current density when the electric motor power demand is high, thus making the FC stack operate under lower temperatures and decreasing its degradation rate. Lifetime was calculated following the end-of-life (EOL) criteria established by the Department of Energy through which an FC stack is considered to have reached the EOL when the voltage decreases by 10% with respect to nominal conditions at a current density of 1 A/cm^2 [53].

The FC durability enhancement is primarily attributed to the reduction in load-change degradation which accounts for most of the overall degradation, lowering from 55% to 10% when restricting the dynamics to 0.001 A/cm^2 s in the case of P-ECMS illustrated in Fig. 14. Consequently, this decline in load-change degradation implies a significant boost in the relevance of other degradation mechanisms, such as start-stop degradation, which could potentially become the most prevalent source of degradation, followed by natural degradation before load-change degradation. This indeed has an impact on how the degradation mechanisms in the FC work, and could potentially help the FC manufacturers design the MEA according to the most expected mechanisms of degradation depending on the stack usage (low or high dynamics). The simulations were conducted on an Intel(R) Xeon(R) CPU E31270 @ 3.40 GHz computer with 16 GB RAM. However, a detailed study of the computational cost of the strategy goes beyond the scope of this paper. Future work will include HiL simulations to test P-ECMS on a dedicated microcontroller.

5.2. Bucarest-Giurgiu driving cycle

The velocity predictor accuracy is also confirmed in the Bucarest-Giurgiu test case, achieving a velocity RMSE of 11.89 km/h (Fig. 15). The second test case for both P-ECMS and A-ECMS utilized the optimal calibrations of k_p and EF_0 obtained for the HDDT cycle. This choice was made to evaluate the robustness of these EMS when exposed

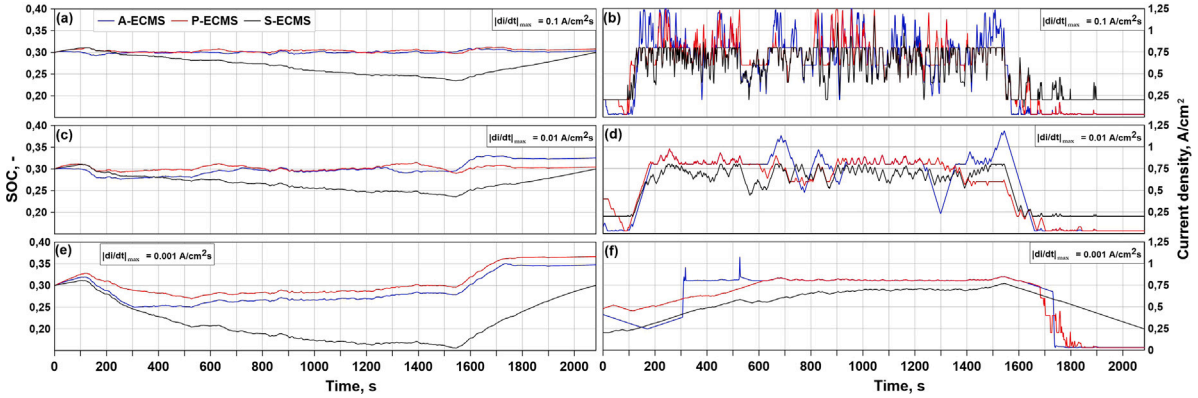

Fig. 8. Comparison of time evolution SOC (a–c–e) and fuel cell current density (b,d,f) for different fuel cell dynamic limitations in the HDDT cycle.

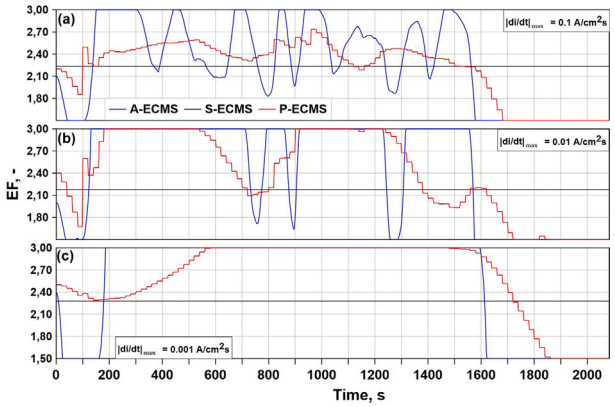

Fig. 9. Comparison of time evolution equivalence factor for different fuel cell dynamic limitations in the HDDT cycle.

to diverse driving circumstances. The HDDT cycle was adopted as the benchmark driving cycle for optimization since it is a standardized cycle that embodies a representative average cycle including a range of driving conditions that could arise in real-life.

From Fig. 16, it is evident that the S-ECMS fails to ensure optimal battery charge sustenance in the Bucarest-Giurgiu test case. The maximum SOC achieved by the S-ECMS is almost 50% for each dynamic limitation case (Fig. 16-a–c–e), which leads to a lower load on the FCS in the latter part of the driving mission (Fig. 16-b–d–f), resulting in a reduced hydrogen consumption (Fig. 17). This consumption is nearly 6% lower than that of the P-ECMS in the high dynamic case but the difference increases when the dynamic limit is reduced (Fig. 17). The behavior from the S-ECMS can only be obtained by knowing the cycle beforehand since the battery is charged preventively when the e-motor power demand is low to increase the overall powertrain efficiency when the power demand is high (at high load the FCS efficiency falls and using it together with the battery lowers the H_2 consumption). This operation, albeit optimal performance-wise, is not realistic and hardly compatible with charge-sustaining modes without a priori knowledge of the driving cycle. Both the P-ECMS and A-ECMS exhibit similar performance characteristics because of a similar power distribution (Fig. 18). Nonetheless, the P-ECMS outperforms the A-ECMS as it can estimate the future velocity profile, thus reducing H_2 consumption by ~0.7–3.2% depending on the $|di/dt|_{max}$. The impact in H_2 consumption when comparing the P-ECMS and the A-ECMS is higher at high dynamics (3.2%) since the FC control is less constrained, thus allowing the vehicle to make full use of the speed forecast. As the dynamic limitation on the FCS increases, this benefit decreases since the evolution of the current density cannot follow the optimal evolution predicted by the P-ECMS, thus implying a penalty in performance. Unlike the HDDT cycle, in this test case, all EMSs exhibit a reduced final SOC tracking error, with the worst case represented by a battery discharge of 2% by the P-ECMS for the $|di/dt|_{max}$ = 0.001 A/cm^2 s (Fig. 19). To achieve these values of SOC at the end of the cycle, both the P-ECMS and the A-ECMS need to bypass the constraint in the dynamics several times to maintain the SOC within the set limits. This implies that having the option to occasionally ignore this limit in both the P-ECMS and the A-ECMS is even more critical in realistic driving conditions and that without this function the charge-sustaining operation would not be possible.

Figs. 20 and 21 confirm that imposing dynamic limitations increases the durability of the FC stack more than twice for each EMS, mainly due to the reduction of load-change degradation. Contrary to the results obtained in the HDDT cycle (Fig. 14), high-power degradation is not negligible, although it is the least relevant. This is mainly due to the fact that during real driving, it may be possible to reach high power demand conditions, thus making the FC stack operate at current densities higher than 1 A/cm^2 (Fig. 16). For brevity, the relative contribution of each degradation source is only illustrated for the P-ECMS in Fig. 21, which highlights the reduction of the weight of load-change degradation from 63% to 23%. When comparing predicted FC durability for the $|di/dt|_{max}$ = 0.01 A/cm^2 s and $|di/dt|_{max}$ = 0.001 A/cm^2 s cases, it can be seen how durability only increases by 6.2%–22% (excluding the S-ECMS case since it is not realistic). This effect is particularly small in the case of the P-ECMS in which the durability only increases by 6.2% and implies a penalty in H_2 consumption of 2.1%. This indicates that for realistic driving with the P-ECMS or the A-ECMS, constraining the FC dynamics to very low levels does not bring significant benefits in terms of durability. Therefore, it may be interesting in terms of the trade-off between performance and durability to consider moderate dynamics ($|di/dt|_{max}$ = 0.01 A/cm^2 s) for real-world driving. Nonetheless, this needs to be complemented by a life cycle assessment or total cost of ownership calculation depending on the cost function to be optimized.

6. Conclusion

This work proposes a P-ECMS suitable for real driving conditions of a heavy-duty FCV and analyzes the impact of imposing FC dynamic limitations both on the FC stack durability and hydrogen consumption. For this purpose, a comprehensive vehicle model has been developed, which includes a validated and optimized FCS model capable of assessing the MEA degradation under various operating conditions. The P-ECMS has been enhanced by integrating an LSTM prediction layer that improves battery SOC sustenance by adapting the equivalence factor according to the difference between the predicted and target SOC. To train the velocity predictor, a realistic driving dataset has been generated with GT-Real Drive using information from the TEN-T routes. Furthermore, a sensitivity analysis of the P-ECMS to the initial equivalence factor and its update gain value has been performed. The

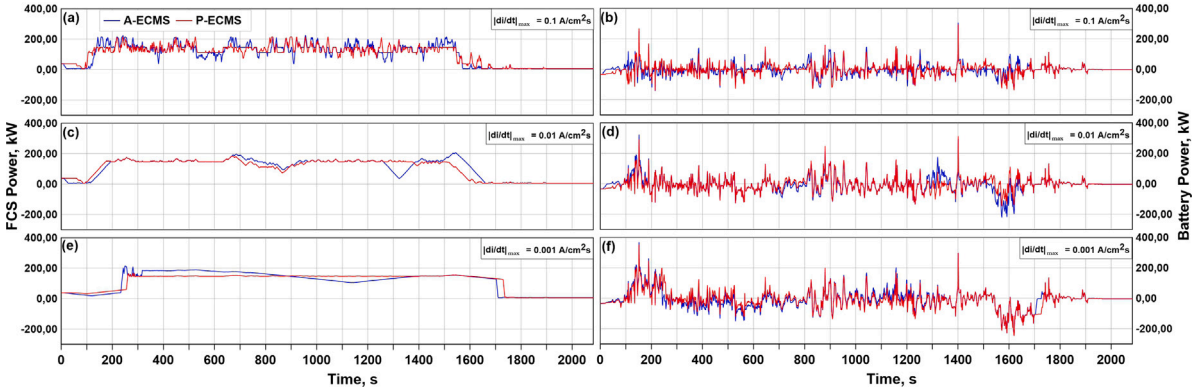

Fig. 10. Comparison of time evolution FCS power (a–c–e) and battery (b,d,f) for different fuel cell dynamic limitations in the HDDT cycle.

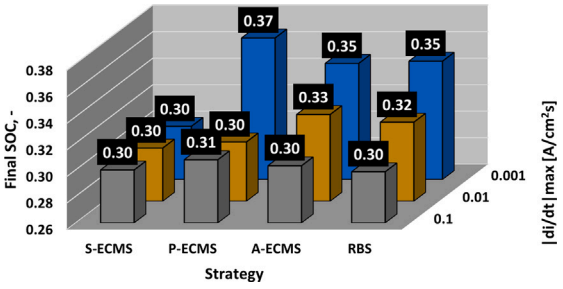

Fig. 11. Terminal SOC evolution as a function of the EMS and the dynamic limitations in the HDDT cycle.

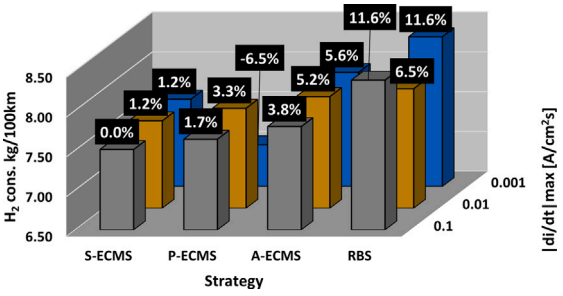

Fig. 12. H_2 consumption evolution as a function of the EMS and the dynamic limitations in the HDDT cycle.

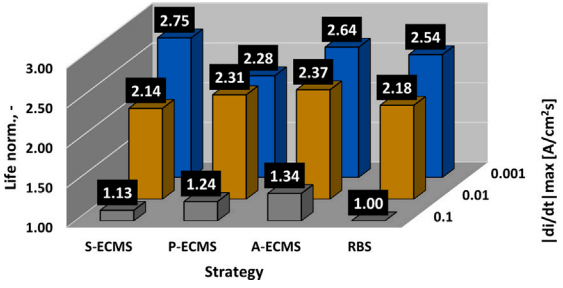

Fig. 13. Normalized FC stack durability (life) evolution as a function of the EMS and the dynamic limitations in the HDDT cycle.

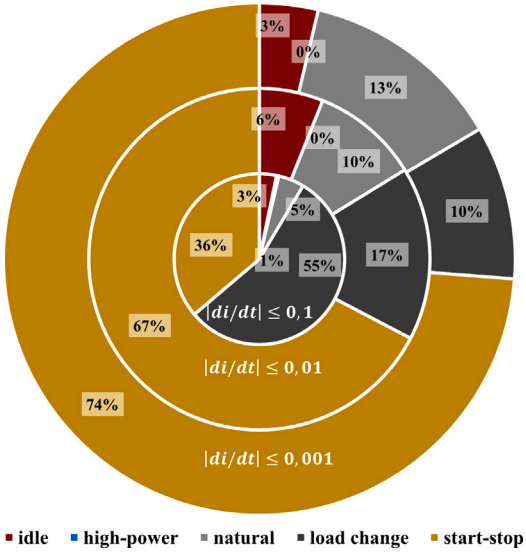

Fig. 14. Degradation source relative effect on FC stack durability for the P-ECMS with different dynamic limitations. |di/dt| is in A/cm^2 s.

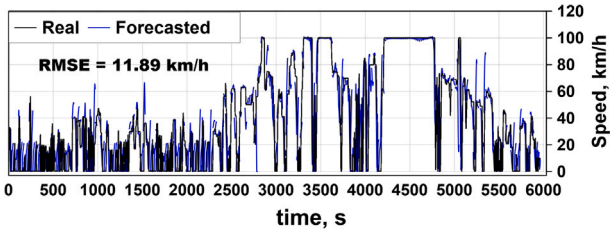

Fig. 15. Speed forecasting in the driving cycle Bucarest-Giurgiu.

P-ECMS has been compared with a conventional A-ECMS, the reference S-ECMS, and an RBS for two different driving cycles and three dynamic restrictions (0.1, 0.01, and 0.001 A/cm^2 s), in terms of battery SOC sustenance, equivalence factor evolution, hydrogen consumption, and FC degradation. The velocity forecasting accuracy has been confirmed by a velocity RMSE of 6.08 km/h and 11.80 km/h for the HDDT and Bucarest-Giurgiu cycles, respectively. Both the P-ECMS and A-ECMS are capable of improving battery SOC sustenance compared to the S-ECMS. However, the P-ECMS achieves a reduction in H_2 consumption ranging from 1.4 to 2% for the HDDT cycle and up to 3% for the realistic driving cycle depending on the dynamic limitation compared

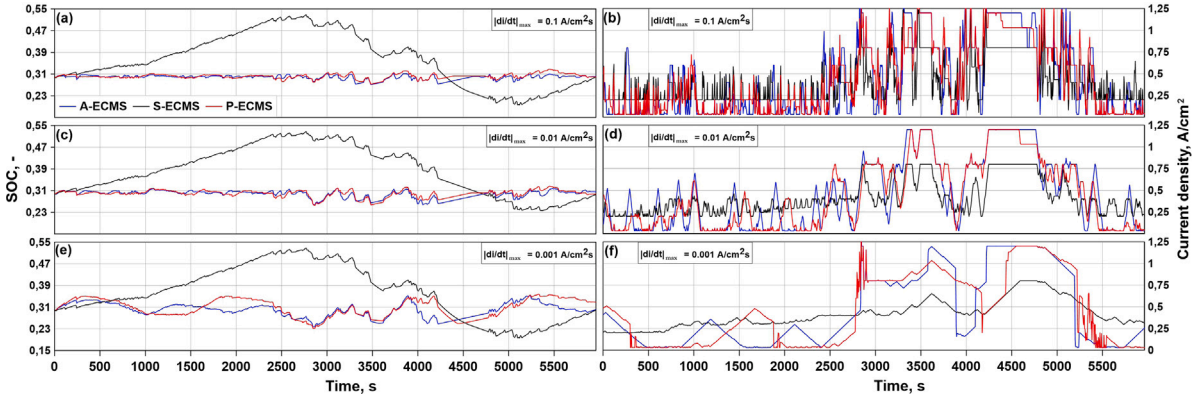

Fig. 16. Comparison of time evolution SOC (a–c–e) and fuel cell current density (b,d,f) for different fuel cell dynamic limitations in the Bucarest-Giurgiu cycle.

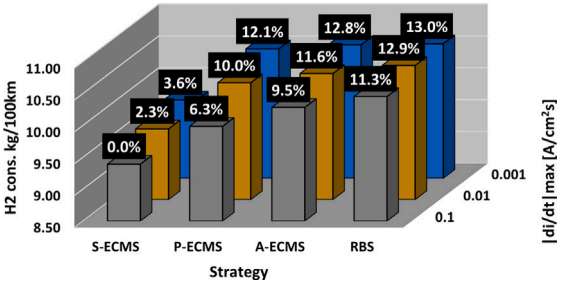

Fig. 17. H_2 consumption evolution as a function of the EMS and the dynamic limitations in the Bucarest-Giurgiu cycle.

to the A-ECMS. When compared to an RBS, fuel consumption is reduced up to 6.1%. Results also showed that increasing the dynamic limitations raised H_2 consumption and FC durability for all the tested strategies. In conclusion, the application of high dynamic limitations results in a shift in the relevance of degradation rate sources. Load-change degradation, which represents a major source of degradation with a low dynamic restriction, becomes a minor factor, with start-stop and low-power degradation becoming more significant. This finding could potentially impact the design process of FC stack manufacturers for FCREx vehicles. Instead of focusing on designing the FC stack inner channels to decrease water management issues in highly-dynamic operations, they may need to prioritize the design of low-degradation start-stop sequences or consider materials that have low degradation under high-voltage conditions.

CRediT authorship contribution statement

M. Piras: Writing – original draft, Visualization, Validation, Software, Investigation, Formal analysis, Data curation. **V. De Bellis:** Writing – review & editing, Supervision, Methodology, Formal analysis, Conceptualization. **E. Malfi:** Writing – review & editing, Visualization, Supervision. **R. Novella:** Writing – review & editing, Supervision, Resources, Project administration, Methodology. **M. Lopez-Juarez:** Writing – review & editing, Visualization, Methodology, Investigation, Formal analysis.

Declaration of competing interest

The authors declare that they have no known competing financial interests or personal relationships that could have appeared to influence the work reported in this paper.

Data availability

Data will be made available on request.

Declaration of Generative AI and AI-assisted technologies in the writing process

During the preparation of this work the authors used Chat-GPT in order to improve language and readability. Chat-GPT was not used to make any content contribution and all the meaningful result and discussion were developed by the authors. After using this tool/service, the authors reviewed and edited the content as needed and take full responsibility for the content of the publication.

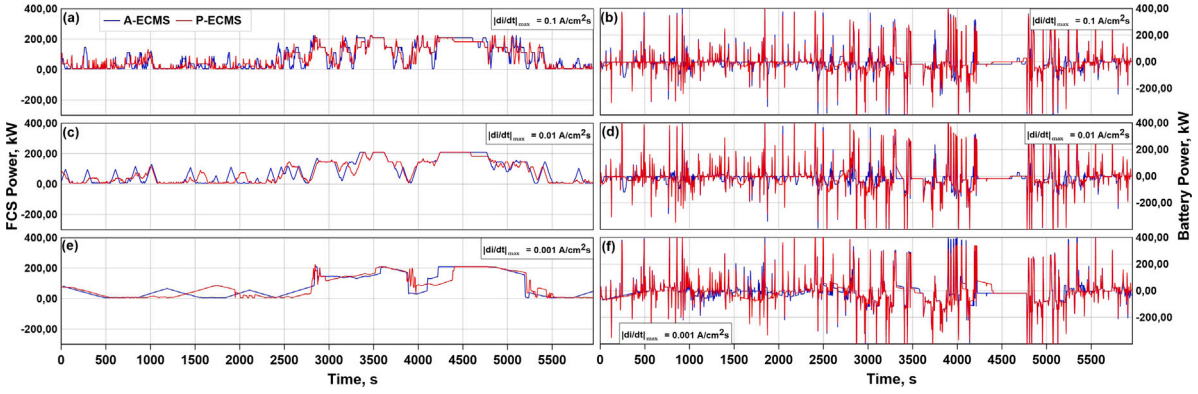

Fig. 18. Comparison of time evolution FCS power (a–c–e) and battery (b,d,f) for different fuel cell dynamic limitations in the Bucarest-Giurgiu cycle.

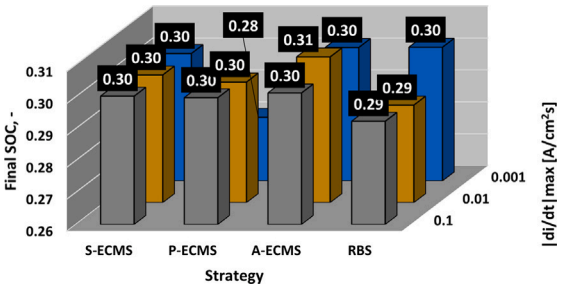

Fig. 19. Terminal SOC evolution as a function of the EMS and the dynamic limitations in the Bucarest-Giurgiu cycle.

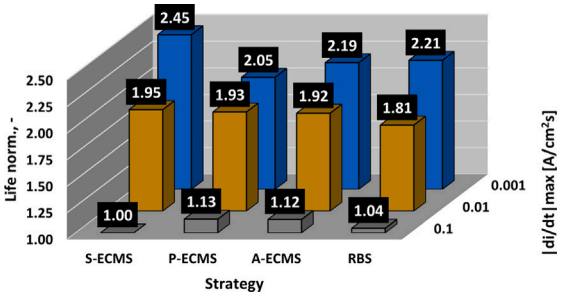

Fig. 20. Normalized FC stack durability (life) evolution as a function of the EMS and the dynamic limitations in the Bucarest-Giurgiu cycle.

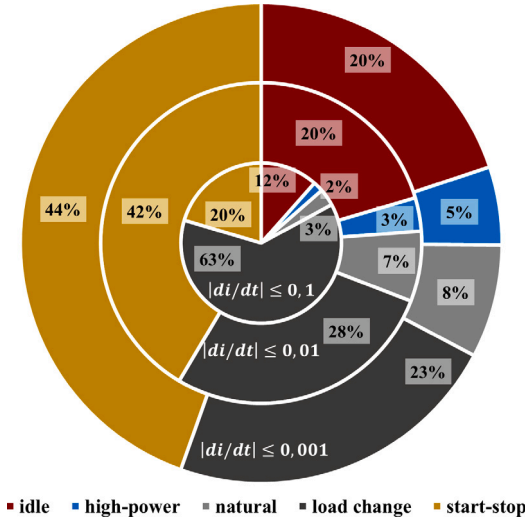

Fig. 21. Degradation source relative effect on FC stack durability for the P-ECMS with different dynamic limitations in the Bucarest-Giurgiu cycle. |di/dt| is in A/cm^2 s.

Acknowledgments

This research is part of the project TED2021-131463B-I00 (DIVERGENT) funded by MCIN/AEI/10.13039/501100011033 and the European Union "NextGenerationEU"/PRTR.

Appendix A. Models' validation

The physical model of the vehicle under study, the Hyundai X-CIENT [33], is implemented in the widely utilized GT-Suite platform.

Table A.5
Cathode temperature and pressure conditions.

T_{cath}, K	p_{cath}, bar
305	1.3
346	1.3
346	2.5

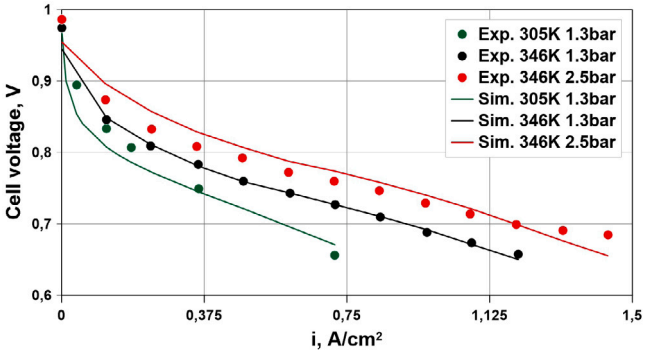

Fig. A.22. Model/experiment comparison of cell voltage against current density for different cathode pressures and temperatures.

Preliminary simulations were performed to evaluate the global model behavior, highlighting a vehicle range consistent with the manufacturer's declared value. This assessment was specifically derived from the HDDT driving cycle and estimated at around 400 km. The validation of the sub-models of fuel cell and its degradation has been carried out and extensively discussed in previous publications [10,11,54]. The main assumptions and results for those sub-models are briefly summarized in this section, while for further details, reference is made to [10,11,54].

A.1. Fuel cell model

The fuel cell model, as described by Eqs. (1)–(5) in the manuscript, was validated involving the simultaneous fitting of three distinct numerical polarization curves to experimental data from [38,39]. This validation encompassed a total of 34 experimental points, conducted under varying pressure and temperature conditions at the cathode (Table A.5):

Calibration of critical parameters, including the reference exchange current density ($i_{0,ref}$), reference ohmic resistance (R_{ohm}), charge transfer coefficient (α), mass transport loss coefficient (C), limiting current density (i_l), and voltage open circuit losses values (V_{OC}), was carried out using the GT-Suite genetic algorithms toolbox. The NSGA-III evolutionary global search genetic algorithm was specifically chosen as the optimization technique, aiming to minimize the overall error between experimental and simulated polarization curve voltages under diverse temperature and pressure conditions. To ensure convergence, a total of 15 solution generations were employed. Beyond the 10–12th generation, the evolution of error between experimental and simulation results reached an asymptotic state. The validation of the model under a wide range of states at the cathode is particularly crucial to simulate the fuel cell under driving cycle conditions, where this is subjected to diverse operational scenarios influenced by external factors and the operation of BoP components. The synthetic validation results, illustrated in Fig. A.22, demonstrate an overall good model accuracy, highlighted by a root mean square deviation of less than 2%. The validated fuel cell stack was incorporated into a comprehensive BoP model that had been previously optimized in a study to which the reader is referred for further discussion [34].

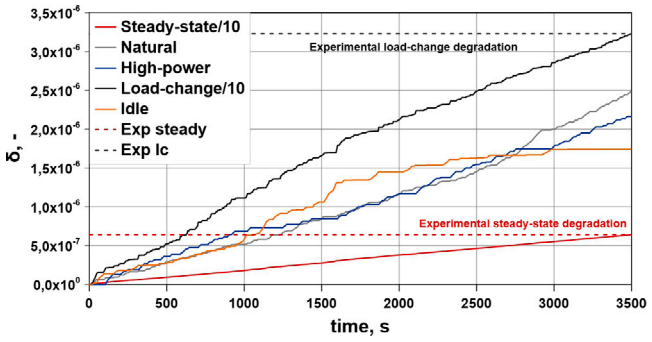

Fig. A.23. Validation results: comparison of experimental [7] degradation rate sources at the end of a real driving cycle with model degradation rate sources. Steady-state degradation comprises low-power, high-power, and natural degradation. Load-change and steady-state voltage loss ratio (δ) evolution were divided by 10.

A.2. Degradation model

The degradation model validation was conducted using the data from [7], involving the simulation of a fuel cell bus under real driving cycle conditions. To perform the validation of the model, the previously described fuel cell model was used. However, the FC model was modified to align its characteristics with the fuel cell stack in [7], featuring 280 cm^2 of active surface area and a comparable power output. Subsequently, this stack was integrated into a balance of plant to ensure that the flow conditions of the FC stack accurately reflected those in a fuel cell vehicle. Following the simulation of a real driving cycle and obtaining the evolution of current density, temperature, as well as cathode and anode relative humidity, the degradation rates of the various sources were evaluated along the driving mission, depicted in Fig. 2, and the final values are compared to the ones advised in [7] (see Fig. A.23).

The validation methodology involved matching the degradation resulting from load-changing cycling, encompassing the contributions of low-power, high-power, and natural degradations, and steady-state operation with the corresponding experimental data. To align the model with experimental results, the model parameters i_{lp} and i_{hp}, of Eqs. (12) and (15), which delineates the transition between degradation conditions. More specifically, i_{lp} signifies the maximum current density for which the low-power/idle degradation mechanism is considered, while i_{hp} represents the minimum current density at which high-power degradation is taken into account. Consequently, they establish the range of current densities within which the scaling functions $\xi_{lp}(i)$ and $\xi_{hp}(i)$ are non-zero, defining the variation of natural degradation with current density. They were calibrated to ensure that the error in the degradation rate for load-changing cycling and at steady-state operation remained below 0.1%, leading to the values of 0.33 A/cm^2 and 1 A/cm^2 for i_{lp} and i_{hp}, respectively. In the end, to assess the adequacy of modeling natural degradation, the total life of the PEMFC stack due to natural degradation was calculated, assuming end-of-life at $\delta = 0.1$ at 1 A/cm^2. In the validation scenario, the degradation rate attributed to natural degradation was $2.57 * 10^{-4}$% V/h, resulting in a lifespan of approximately 39'600 h, consistent with DOE 2020 targets [53]. For further details reader is referred to [11].

References

[1] Samsun RC, Rex M, Antoni L, Stolten D. Deployment of fuel cell vehicles and hydrogen refueling station infrastructure: A global overview and perspectives. Energies 2022;15. http://dx.doi.org/10.3390/en15144975.

[2] Hydrogen roadmap Europe : a sustainable pathway for the European energy transition. Publications Office; 2019, http://dx.doi.org/10.2843/341510.

[3] on Clean Transportation IC. Vision 2050: A strategy to decarbonize the global transport sector by mid-century. 2020.

[4] Song K, Ding Y, Hu X, Xu H, Wang Y, Cao J. Degradation adaptive energy management strategy using fuel cell state-of-health for fuel economy improvement of hybrid electric vehicle. Appl Energy 2021;285:116413. http://dx.doi.org/10.1016/j.apenergy.2020.116413.

[5] Li J, Yang L, Yang Q, Wei Z, He Y, Lan H. Degradation adaptive energy management with a recognition-prediction method and lifetime competition-cooperation control for fuel cell hybrid bus. Energy Convers Manage 2022;271:116306. http://dx.doi.org/10.1016/J.ENCONMAN.2022.116306.

[6] Luca R, Whiteley M, Neville T, Shearing PR, Brett DJ. Comparative study of energy management systems for a hybrid fuel cell electric vehicle - A novel mutative fuzzy logic controller to prolong fuel cell lifetime. Int J Hydrogen Energy 2022;47:24042–58. http://dx.doi.org/10.1016/J.IJHYDENE.2022.05.192.

[7] Pei P, Chang Q, Tang T. A quick evaluating method for automotive fuel cell lifetime. Int J Hydrogen Energy 2008;33(14):3829–36. http://dx.doi.org/10.1016/j.ijhydene.2008.04.048.

[8] Quan S, Wang Y-X, Xiao X, He H, Sun F. Real-time energy management for fuel cell electric vehicle using speed prediction-based model predictive control considering performance degradation. Appl Energy 2021;304:117845. http://dx.doi.org/10.1016/j.apenergy.2021.117845.

[9] Peng F, Zhao Y, Chen T, Zhang X, Chen W, Zhou D, Li Q. Development of robust suboptimal real-time power sharing strategy for modern fuel cell based hybrid tramways considering operational uncertainties and performance degradation. Appl Energy 2018;226:503–21. http://dx.doi.org/10.1016/j.apenergy.2018.05.092.

[10] Desantes J, Novella R, Pla B, Lopez-Juarez M. Effect of dynamic and operational restrictions in the energy management strategy on fuel cell range extender electric vehicle performance and durability in driving conditions. Energy Convers Manage 2022;266(X):115821. http://dx.doi.org/10.1016/j.enconman.2022.115821.

[11] Desantes J, Novella R, Pla B, Lopez-Juarez M. A modeling framework for predicting the effect of the operating conditions and component sizing on fuel cell degradation and performance for automotive applications. Appl Energy 2022;317:119137. http://dx.doi.org/10.1016/j.apenergy.2022.119137.

[12] Zhu Z, Zeng L, Chen L, Zou R, Cai Y. Fuzzy adaptive energy management strategy for a hybrid agricultural tractor equipped with HMCVT. Agriculture 2022;12:1986. http://dx.doi.org/10.3390/agriculture12121986.

[13] Shi D, Liu S, Cai Y, Wang S, Li H, Chen L. Pontryagin's minimum principle based fuzzy adaptive energy management for hybrid electric vehicle using real-time traffic information. Appl Energy 2021;286. http://dx.doi.org/10.1016/j.apenergy.2021.116467.

[14] Ravey A, Blunier B, Miraoui A. Control strategies for fuel-cell-based hybrid electric vehicles: From offline to online and experimental results. IEEE Trans Veh Technol 2012;61:2452–7. http://dx.doi.org/10.1109/TVT.2012.2198680.

[15] Onori S, Serrao L, Rizzoni G. Adaptive equivalent consumption minimization strategy for hybrid electric vehicles. In: ASME 2010 dynamic systems and control conference, DSCC2010, Vol. 1. 2010, p. 499–505. http://dx.doi.org/10.1115/DSCC2010-4211.

[16] Hussain S, Ali MU, Park GS, Nengroo SH, Khan MA, Kim HJ. A real-time bi-adaptive controller-based energy management system for battery–supercapacitor hybrid electric vehicles. Energies 2019;12:4662. http://dx.doi.org/10.3390/EN12244662, 2019, Vol. 12, Page 4662.

[17] Yang D, Wang L, Yu K, Liang J. A reinforcement learning-based energy management strategy for fuel cell hybrid vehicle considering real-time velocity prediction. Energy Convers Manage 2022;274:116453. http://dx.doi.org/10.1016/j.enconman.2022.116453.

[18] Min D, Song Z, Chen H, Wang T, Zhang T. Genetic algorithm optimized neural network based fuel cell hybrid electric vehicle energy management strategy under start-stop condition. Appl Energy 2022;306:118036. http://dx.doi.org/10.1016/j.apenergy.2021.118036.

[19] Sun C, Hu X, Moura SJ, Sun F. Velocity predictors for predictive energy management in hybrid electric vehicles. IEEE Trans Control Syst Technol 2015;23(3):1197–204. http://dx.doi.org/10.1109/TCST.2014.2359176.

[20] Zhou Y, Ravey A, Péra M-C. Multi-mode predictive energy management for fuel cell hybrid electric vehicles using Markov driving pattern recognizer. Appl Energy 2020;258:114057. http://dx.doi.org/10.1016/j.apenergy.2019.114057.

[21] Sun X, Zhou Y, Zhang X, Huang L, Lian J. Real-time optimal EMS of adaptive charge sustenance for fuel cell hybrid buses based on driving characteristics recognition. Energy Convers Manage 2022;254. http://dx.doi.org/10.1016/j.enconman.2021.115192.

[22] Shen P, Zhao Z, Zhan X, Li J, Guo Q. Optimal energy management strategy for a plug-in hybrid electric commercial vehicle based on velocity prediction. Energy 2018;155:838–52. http://dx.doi.org/10.1016/j.energy.2018.05.064.

[23] Ferrara A, Okoli M, Jakubek S, Hametner C. Energy management of heavy-duty fuel cell electric vehicles: Model predictive control for fuel consumption and lifetime optimization. IFAC-PapersOnLine 2020;53(2):14205–10. http://dx.doi.org/10.1016/j.ifacol.2020.12.1053, 21st IFAC World Congress.

[24] Guo X, Yan X, Chen Z, Meng Z. Research on energy management strategy of heavy-duty fuel cell hybrid vehicles based on dueling-double-deep Q-network. Energy 2022;260:125095. http://dx.doi.org/10.1016/j.energy.2022.125095.

[25] Lin X, Xu X, Lin H. Predictive-ECMS based degradation protective control strategy for a fuel cell hybrid electric vehicle considering uphill condition. eTransportation 2022;12:100168. http://dx.doi.org/10.1016/j.etran.2022.100168.
[26] Lin X, Wang Z, Wu J. Energy management strategy based on velocity prediction using back propagation neural network for a plug-in fuel cell electric vehicle. Int J Energy Res 2021;45(2):2629–43. http://dx.doi.org/10.1002/er.5956, arXiv:https://onlinelibrary.wiley.com/doi/pdf/10.1002/er.5956.
[27] Liu Y, Li J, Chen Z, Qin D, Zhang Y. Research on a multi-objective hierarchical prediction energy management strategy for range extended fuel cell vehicles. J Power Sources 2019;429:55–66. http://dx.doi.org/10.1016/j.jpowsour.2019.04.118.
[28] Li X, Wang Y, Yang D, Chen Z. Adaptive energy management strategy for fuel cell/battery hybrid vehicles using pontryagin's minimal principle. J Power Sources 2019;440:227105. http://dx.doi.org/10.1016/j.jpowsour.2019.227105.
[29] Zhou Y, Li H, Ravey A, Péra M-C. An integrated predictive energy management for light-duty range-extended plug-in fuel cell electric vehicle. J Power Sources 2020;451:227780. http://dx.doi.org/10.1016/j.jpowsour.2020.227780.
[30] Zhang Z, He H, Guo J, Han R. Velocity prediction and profile optimization based real-time energy management strategy for plug-in hybrid electric buses. Appl Energy 2020;280. http://dx.doi.org/10.1016/j.apenergy.2020.116001.
[31] Xie S, Hu X, Xin Z, Brighton J. Pontryagin's minimum principle based model predictive control of energy management for a plug-in hybrid electric bus. Appl Energy 2019;236:893–905. http://dx.doi.org/10.1016/J.APENERGY.2018.12.032.
[32] Li M, Yan M, He H, Peng J. Data-driven predictive energy management and emission optimization for hybrid electric buses considering speed and passengers prediction. J Clean Prod 2021;304. http://dx.doi.org/10.1016/J.JCLEPRO.2021.127139.
[33] FuelCellsWorks. World's first fuel cell heavy-duty truck, Hyundai XCIENT Fuel Cell, heads to Europe for commercial use. 2020.
[34] Molina S, Novella R, Pla B, Lopez-Juarez M. Optimization and sizing of a fuel cell range extender vehicle for passenger car applications in driving cycle conditions. Appl Energy 2021;285. http://dx.doi.org/10.1016/j.apenergy.2021.116469.
[35] Desantes JM, Novella R, Pla B, Lopez-Juarez M. Impact of fuel cell range extender powertrain design on greenhouse gases and NOX emissions in automotive applications. Appl Energy 2021;302. http://dx.doi.org/10.1016/j.apenergy.2021.117526.
[36] Springer TE, Zawodzinski TA, Gottesfeld S. Polymer electrolyte fuel cell model. J Electrochem Soc 1991;138:208.
[37] Murschenhofer D, Kuzdas D, Braun S, Jakubek S. A real-time capable quasi-2D proton exchange membrane fuel cell model. Energy Convers Manage 2018;162:159–75. http://dx.doi.org/10.1016/J.ENCONMAN.2018.02.028.
[38] Corbo P, Migliardini F, Veneri O. Experimental analysis and management issues of a hydrogen fuel cell system for stationary and mobile application. Energy Convers Manage 2007;48:2365–74. http://dx.doi.org/10.1016/J.ENCONMAN.2007.03.009.
[39] Corbo P, Migliardini F, Veneri O. Experimental analysis of a 20 kWe PEM fuel cell system in dynamic conditions representative of automotive applications. Energy Convers Manage 2008;49:2688–97. http://dx.doi.org/10.1016/J.ENCONMAN.2008.04.001.
[40] Knights S. Polymer electrolyte membrane and direct methanol fuel cell technology: 6 - operation and durability of low temperature fuel cells. Woodhead Publishing Limited; 2012, p. 137–77. http://dx.doi.org/10.1533/9780857095473.2.137.
[41] Bi W, Fuller TF. Temperature effects on PEM fuel cells PtC catalyst degradation. J Electrochem Soc 2008;155(2):B215. http://dx.doi.org/10.1149/1.2819680.
[42] Dutta M, Jia N, Lu S, Colbow V, Wessel S. Effects of upper potential dwell time, transients and relative humidity on PEM fuel cell cathode catalyst degradation. In: The electrochemical society 217th meeting (c). 2010.
[43] Onori S, Serrao L, Rizzoni G. Adaptive equivalent consumption minimization strategy for hybrid electric vehicles. In: ASME 2010 dynamic systems and control conference, DSCC2010, Vol. 1. American Society of Mechanical Engineers Digital Collection; 2011, p. 499–505. http://dx.doi.org/10.1115/DSCC2010-4211.
[44] Piras M, De Bellis V, Malfi E, Novella R, Lopez-Juarez M. Adaptive ECMS based on speed forecasting for the control of a heavy-duty fuel cell vehicle for real-world driving. Energy Convers Manage 2023;289:117178. http://dx.doi.org/10.1016/j.enconman.2023.117178.
[45] Yu Y, Si X, Hu C, Zhang J. A review of recurrent neural networks: Lstm cells and network architectures. Neural Comput 2019;31:1235–70. http://dx.doi.org/10.1162/neco_a_01199.
[46] Hochreiter S, Schmidhuber J. Long short-term memory. Neural Comput 1997;9:1735–80. http://dx.doi.org/10.1162/NECO.1997.9.8.1735.
[47] Lin X, Wu J, Wei Y. An ensemble learning velocity prediction-based energy management strategy for a plug-in hybrid electric vehicle considering driving pattern adaptive reference SOC. Energy 2021;234. http://dx.doi.org/10.1016/j.energy.2021.121308.
[48] Zeng T, Zhang C, Zhang Y, Deng C, Hao D, Zhu Z, Ran H, Cao D. Optimization-oriented adaptive equivalent consumption minimization strategy based on short-term demand power prediction for fuel cell hybrid vehicle. Energy 2021;227. http://dx.doi.org/10.1016/j.energy.2021.120305.
[49] Han S, Zhang F, Xi J, Ren Y, Xu S. Short-term vehicle speed prediction based on convolutional bidirectional LSTM networks. In: 2019 IEEE intelligent transportation systems conference (ITSC). 2019, p. 4055–60. http://dx.doi.org/10.1109/ITSC.2019.8917345.
[50] Zhang F, Xi J, Langari R. Real-time energy management strategy based on velocity forecasts using V2V and V2I communications. IEEE Trans Intell Transp Syst 2017;18(2):416–30. http://dx.doi.org/10.1109/TITS.2016.2580318.
[51] Chen D, Kim Y, Stefanopoulou AG. Predictive equivalent consumption minimization strategy with segmented traffic information. IEEE Trans Veh Technol 2020;69:14377–90. http://dx.doi.org/10.1109/TVT.2020.3034552.
[52] Luciani S, Tonoli A. Control strategy assessment for improving PEM fuel cell system efficiency in fuel cell hybrid vehicles. Energies 2022;15. http://dx.doi.org/10.3390/en15062004.
[53] DoE - Department of Energy. DOE Technical Targets for Polymer Electrolyte Membrane Fuel Cell Components.
[54] Novella R, la Morena JD, Lopez-Juarez M, Nidaguila I. Effect of differential control and sizing on multi-FCS architectures for heavy-duty fuel cell vehicles. Energy Convers Manage 2023;293:117498. http://dx.doi.org/10.1016/j.enconman.2023.117498.